Holey Carbon Nanotubes from Controlled Air Oxidation

Yi Lin,[*,1,2] *Michael R. Funk,*[2,3] *Caroline J. Campbell,*[1] *Jae-Woo Kim,*[1] *Xiaogang Han,*[4] *Steven D. Lacey,*[4] *Liangbing Hu,*[4] *and John W. Connell*[3]

[1]National Institute of Aerospace, 100 Exploration Way, Hampton, Virginia 23666, [2]Department of Applied Science, The College of William and Mary, Williamsburg, VA 23185, and [3]Advanced Materials and Processing Branch, NASA Langley Research Center, Hampton, Virginia 23681-2199, [4]Department of Materials Science and Engineering, University of Maryland, College Park, MD 20742;

[*]To whom correspondence should be addressed: yi.lin-1@nasa.gov

KEYWORDS: holey carbon nanotubes, catalyst-free, porous carbon, air oxidation, supercapacitors

ABSTRACT

Defects in various nanomaterials are often desirable to enable enhanced functional group attachments and attain properties that are not available with their intact counterparts. A new paradigm in the defective low-dimensional carbon nanomaterials is to create holes on the graphitic surfaces via partial etching. For example, holey graphene, graphene sheets with through-thickness holes, was synthesized using several different partial etching approaches and found useful for various applications such as field-effect transistors, sensors, energy storage devices, and separation membranes. In these applications, the presence of holes led to unique advantages, such as bandgap widening, chemical functionalization of hole edges, improved through-the-thickness ion transport with lowered tortuosity, and improved accessible surface area. Here, we present a facile method to prepare holey carbon nanotubes via controlled air oxidation. Although no additional catalyst was added, the residual iron nanoparticles from nanotube growth encapsulated in the nanotube cavity significantly contributed to the hole generation through the nanotube walls. The holey carbon nanotube products exhibited enhanced surface area, pore volume, and oxygen-containing functional groups, which led to their much enhanced electrochemical capacitive properties. Synthesis and characterization details of this novel class of holey carbon nanomaterials are presented, and their potential applications are discussed.

Introduction

Low-dimensional carbon nanomaterials, especially graphene and carbon nanotubes (CNTs), are known for their excellent mechanical, thermal, electrical, and electronic properties.[1-3] These properties of carbon nanomaterials, in combination with their high surface area, have enabled many applications such as energy storage, sensing, gas storage, waste adsorption, etc. However, bulk carbon nanomaterials have a tendency to aggregate due to the van der Waals attractions between the adjacent conjugated graphitic carbon surfaces, making it challenging to take full advantage of the active surfaces. Various strategies have been proposed to circumvent this problem. For example, creating physical space in between the graphitic surfaces to form porous carbon nanomaterials, such as CNT aerogels or graphene foams, significantly improved their usable surface area, resulting in a large increase in their performance in the above-mentioned applications.[4-11]

Recently, it was shown that an alternative method to improve accessible surface area is to form holes on the graphitic carbon surfaces. For instance, there have been reports on the so-called "holey graphene" materials, where the graphene sheets exhibited through-thickness nanometer-sized holes.[5,12-22] For energy storage applications, intact graphene sheets tend to tightly restack in the electrode architecture, resulting in high ion tortuosity and thus hindering the effectiveness of electrochemistry. The presence of holes in holey graphene sheets significantly enhances ion transport through the graphitic planes in much less tortuous routes. As a result, this approach enables more surface atoms to be effectively accessible in the electrochemical processes although no addition surface area was created in the case of holey graphene vs. graphene.[15,16,20,21] In addition, these holes can be viewed as newly created "surface edges". Increased edge atoms, because of their accessibility and enhanced reactivity, may not only

further enhance the electrochemical performance, but also benefit other applications such as sensors[14,23,24] and separation membranes.[25-27]

Many strategies, such as the use of strong oxidative acid,[15,16,20] catalytic oxidation,[17-19] or direct heating in air,[21,22] have been reported as ways to create holes on graphene sheets. Despite the differences in the chemistry, the key theme in common is the partial etching of lateral surfaces of the graphitic carbon.[13] It is conceivable that similar approaches with certain modification should be also applicable to CNTs because they are also made of graphitic surfaces. Inspired by our previous work on holey graphene,[13,18,21,22] here we demonstrate a facile strategy to create holes on the sidewalls of multi-walled CNTs (MWCNTs) via controlled thermal oxidation in air without additional solvent or reagents. Although no external catalyst was used, the catalytic residue from MWCNT growth encapsulated in the nanotube cavity contributed to the hole generation by catalyzing the gasification of nanotube wall carbons. The hole opening on the nanotube sidewall resulted in increased physical surface area, pore volume, and oxygen functional group content. The combined properties of these "holey carbon nanotubes" (hCNTs) led to significant improvement in their electrochemical capacitances in comparison to their pristine, unoxidized counterparts.

Experimental Section

Materials. MWCNTs (batch# UK115b) with a diameter range of ~ 20 – 150 nm were purchased from the University of Kentucky. Potassium hydroxide (KOH; ≥85.0%; Certified ACS Grade) and hydrochloric acid (HCl; 36.5-38.0% wt/wt; Certified ACS Plus Grade) were purchased from Fisher Scientific. Nafion solutions (5%, Type DE-521, Lot No.: SGA03–004) were purchased from Fuel Cell Store.

Measurements. Scanning electron microscopy (SEM) and transmission electron microscopy (TEM) images were acquired using a Hitachi S-5200 field-emission SEM system at an acceleration voltage of 30 kV under the secondary electron (SE) and transmitted electron (TE) modes, respectively. Raman spectroscopy measurements were performed using a Thermo-Nicolet-Almega Dispersive Raman Spectrometer with 785 nm excitation. Nitrogen adsorption-desorption isotherms and the corresponding Brunauer–Emmett–Teller (BET) surface area values and Barrett–Joyner–Halenda (BJH) pore characteristics were acquired on a Quantachrome Nova 2200e Surface Area and Pore Size Analyzer system using a 9-mm bulbless cell. Thermogravimetric analysis (TGA) data were obtained using a TA TGA-Q50 Thermogravimetric Analyzer system by heating the specimens to 800 °C in air at a ramp rate of 10 °C/min. X-ray photoelectron spectroscopy (XPS) data were collected on a Kratos Axis 165 X-ray photoelectron spectrometer operating in hybrid mode using monochromatic Al Kα X-rays (1486.7 eV).

Synthesis of hCNTs. In a typical reaction (**Scheme 1**), MWCNT powder (100 mg) was placed in an alumina crucible and heated in an open-ended tube furnace (Thermolyne 21100; temperatures reported are after calibration) with a ramp rate of ~10 °C/min and held isothermally at a set temperature (typically between 380 and 540 °C) for a given period of time. In the purification step, 6 M HCl (20 mL) was added to the heat treated nanotube solid at room temperature and the mixture was stirred for ~1 h. The slurry was then filtered, and the solid was repeatedly washed with deionized water, and dried in vacuum at 60 °C overnight to yield hCNTs.

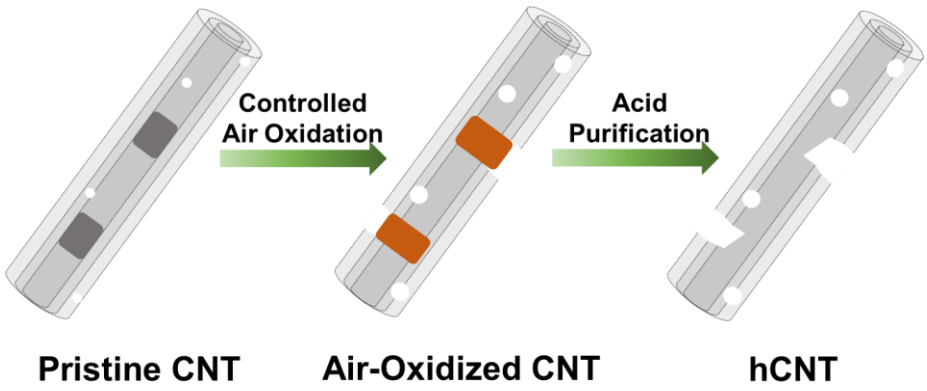

Scheme 1. Facile preparation of hCNTs via controlled air oxidation followed by purification. The grey-colored encapsulates in pristine CNT (MWCNT; left) refer to residual iron catalyst nanoparticles from nanotube growth, which were converted into iron oxide after air oxidation (middle) and removed via acid wash to yield hCNT (right).

Electrochemical Studies. Electrochemical measurements were carried out in a three-electrode configuration with a BioLogic VMP3 electrochemical station. Counter and reference electrodes were a Pt wire and Ag/AgCl (saturated with 3.5 M KCl), respectively. The electrolyte solution (6 M KOH) was purged with argon for at least 20 min before use. In a typical procedure to prepare a working electrode, a sample of interest was dispersed in a dilute Nafion solution (Nafion : ethanol : water = 4:16:80 by volume) at 1 mg/mL and bath sonicated for 30 min to form a homogeneous ink. A 10 µL drop of the ink was carefully placed on a 3-mm diameter glassy carbon electrode surface. The electrode was then placed in an oven heated at 80 °C for at least 2 h. After 2 cyclic scans at 100 mV/s, cyclic voltammetry (CV) was recorded at scanning rates consecutively at 10, 20, 50, 100, 200, 500, and 1000 mV/s. Galvanostatic charge-discharge properties were subsequently recorded on the same electrode at 0.5, 1, 2, and 5 A/g, each for 1 cycle, and 10 A/g for 2 cycles.

Results and Discussion

CNTs used in this work were MWCNTs of several micrometers long with a broad diameter distribution (~20 – 150 nm) that were synthesized via chemical vapor deposition (CVD). Although the pristine nanotubes appeared mostly intact, it is known that the CVD-grown MWCNTs exhibited abundant surface defects distributed along the nanotube length.[28] Some segments of the inner cavities of most nanotubes were encapsulated with residual metallic iron catalysts that consisted of ~6.4% of the total weight according to TGA (ash content ~8.9%).

hCNTs were prepared in a facile two-step procedure as shown in **Scheme 1**. The first step was controlled air oxidation, in which the pristine MWCNTs were heated in an open-ended tube furnace to initiate carbon oxidation and kept isothermally at a set temperature to allow further reaction. The second step was purification, in which the exposed catalysts that were originally encapsulated in the nanotube inner cavity were removed by room temperature acid wash. The controlled air oxidation step was the key to the formation of holes through the nanotube wall, while the purification step using a non-oxidative acid was designed to only remove the exposed catalysts with no significant effect on the hole morphology. Air oxidation followed by acid wash was previously used in the selective removal of graphitic nanoparticle-encapsulated metal catalysts for purification of carbon nanotubes.[29-31] The air oxidation conditions used in this work were optimized for hole generation rather than maintaining the nanotube integrity in those purification attempts (typically low temperature with short durations).

A typical example of an air-oxidized MWCNT (from 430 °C/3 h) is shown in **Figure 1**, which are electron microscopy images of the same nanotube under both secondary (SE; revealing surface features) and transmitted electron (TE; revealing through-thickness features) modes. Several areas (lateral sizes < 15 nm; highlighted in blue) were identified in the SE mode

image (Figure 1a) as shallow pits on the nanotube surfaces. These pits were likely from the direct air oxidation of the external graphitic wall, most likely started from defective surface carbons, similar to the previously reported catalyst-free formation of holes on graphene sheets.[21,22] For the larger-sized holes (lateral sizes > 30 nm) formed through the nanotube wall (highlighted in red) identified in the TE mode image (Figure 1b), each of them was associated with a catalytic iron-containing nanoparticle, indicating the formation was through the catalytic oxidation with these nanoparticles. This finding was consistent with the previous reports on the formation of holey graphene and holey carbon nanotubes using catalytic additives such as noble metallic nanoparticles[18] and iron oxide nanoparticles,[32] except for the iron-containing catalysts here were intrinsically present from the synthesis of the MWCNTs.

Mechanistically, during oxidation, surface defect carbons on the external nanotube wall were first oxidized and gasified into CO or CO_2, forming small diameter shallow holes, as supported by the microscopy images of air-oxidized MWCNTs obtained at moderate heating conditions, i.e., lower temperature and/or shorter duration (more discussions later). With the progressive oxidation, some holes penetrated through the entire nanotube wall structure, exposing the nanotube inner cavity and thus the encapsulated iron-containing catalysts to oxygen access even when they were distant from the opening. The catalytic oxidation then started from the inner wall carbons adjacent to the iron-containing particles, which subsequently migrated with carbon removal to leave "trails". This led to holes that became much larger than the catalyst nanoparticles themselves and the nanotube wall became severely etched. Sometimes the trails happened to move along the nanotube peripheral around the cross-section (an example is highlighted with an arrow in Figure 1) that may eventually lead to nanotube shortening, which is an extreme case of hole formation.

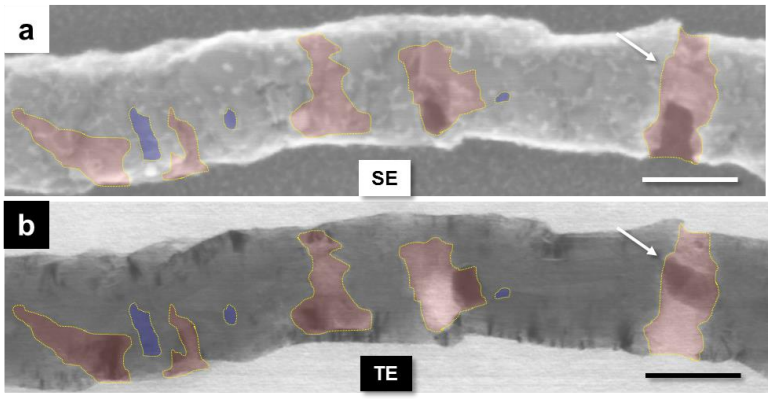

Figure 1. Typical microscopy images on the hole formation on MWCNTs after air oxidation (430 °C/ 3 h). (a) and (b) are images of the same nanotube segment under secondary (SE) and transmitted electron (TE) mode, respectively. Highlighted in red are holes formed through the catalytic effect of nanotube-encapsulated iron nanoparticles, while highlighted in blue are regions that were likely directly oxidized with no catalytic assistance. The arrows point to a catalytically oxidized area that may lead to nanotube shortening. Scale bars = 50 nm.

The extent of the hole formation, herein referred to as the "hole yield", was conveniently monitored by the sample weight loss after heating, which increased with temperature and duration of the heating. For example, at a set temperature of 430 °C, the hole yields for heating durations of 1, 3, and 10 h were 8.4, 24.4, and 50.5%, respectively (**Table 1**). Increasing the set temperature to 480 °C with 1 h duration resulted in a hole yield of 37%. The carbon removal rate rapidly increased at this temperature or higher, when graphitic carbon also became vulnerable to gasification. At this time, the "hole yield" values had more contributions from the loss of nanotubes in their entirety, and thus no longer accurately represent the extent of hole formation. Consistently, long heating durations at these temperatures (e.g. 480 °C/10 h, or 540 °C/1 h) resulted in complete carbon oxidation, with only red-colored iron oxide residue left behind.

Table 1. Physical and electrochemical properties of hCNTs.

	Hole Yield (%)	TGA Ash Content (%)	O at%[a]	D:G Ratio from Raman	BET Surface Area (m^2/g)	BJH Pore Volume (cm^3/g)	Specific Capacity C_m (F/g)[b]
Pristine	N/A	8.9	2	0.34	33.4	0.199	2.9
380°C/10 h	6.3	2	2.6	0.40	31.9	0.166	3.8
430°C/1 h	8.4	3.3	3.2	0.35	59.0	0.205	2.9
430°C/3 h	24.4	1.8	4.4	0.43	41.8	0.215	4.2
430°C/10 h	50.5	1.0	3.6	0.43	56.1	0.246	6.3
480°C/1 h	37	2.6	5.2	0.41	75.7	0.289	4.6
540°C/0.3 h	61.9	2.3	2.5	0.39	39.3	0.255	4.7

[a] Calculated based on carbon and oxygen atomic ratios obtained from XPS survey data.
[b] Obtained from galvanometric charge-discharge data at a current density of 1 A/g.

Purified hCNTs were obtained after effective removal of the exposed catalyst residue using a non-oxidative acid (6 M HCl) at room temperature. Unlike the as-oxidized nanotube samples (e.g. Figure 1), the holes for purified hCNTs were all free from residual catalyst nanoparticles (**Figure 2**). Under a relatively mild condition such as 430 °C/1 h (designated as $hCNT_{430\text{-}1}$), the nanotubes were moderately etched, exhibiting some shallow pits (~10 - 30 nm in diameter) mostly on the surfaces and occasionally some penetrating through the tubular wall (Figure 2a-d). There was a reduction in the residual catalyst content (TGA ash content ~3.3%) after acid purification. This suggests that there was a moderate exposure of the iron-containing particles encapsulated in the nanotube inner cavity after the air oxidation. In a control experiment, the TGA ash content of the pristine nanotubes without air oxidation but after the same acid treatment step was as high as ~8%. Increasing the air oxidation time to 10 h at the same set temperature (430 °C) resulted in much higher hole yield (~50%). Consistently, there was more severe etching of the nanotubes. As shown in Figure 2e-h, large-sized holes over 30 nm in diameter were found along the nanotube body. Some circular-shaped pits penetrated

through the nanotube walls; sometimes a large portion of the wall was missing. The TGA ash contents of the $hCNT_{430\text{-}10}$ sample were significantly lower (~1%) than $hCNT_{430\text{-}1}$, suggesting that most residual catalysts were removed because the nanotube inner cavity was effectively exposed after prolonged air oxidation.

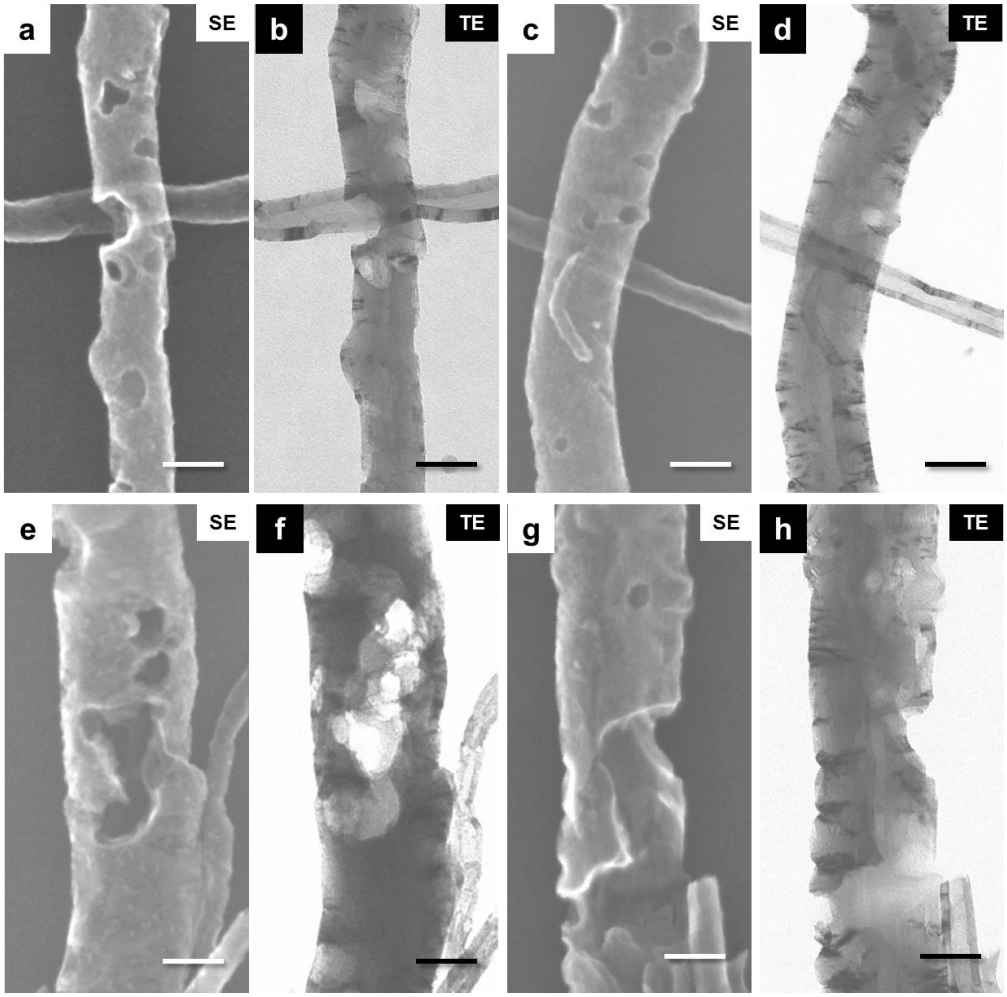

Figure 2. Typical microscopy images of (a-d) $hCNT_{430\text{-}1}$ and (e-h) $hCNT_{430\text{-}10}$. Shown in (a,c,e,g) are images taken under the SE mode, while (b,d,f,h) show the same nanotubes but under the TE mode. Scale bars = 50 nm.

Microscopy investigations suggested that most hCNTs obtained in this work (Table 1) were of tens of μm long and highly entangled, similar to the pristine MWCNTs. Therefore, it was extremely challenging to accurately account for the change in the nanotube length. However, hCNTs with high hole yields (>50%) did exhibit qualitatively more presence of shortened nanotubes (< 1 μm) that were likely from the catalytic cutting (i.e., "extreme hole generation") as previously discussed.

XPS survey data of purified hCNTs suggested that the oxygen contents increased from the pristine MWCNT sample, and generally increased with the hole yield at moderate temperatures (< 480 °C) when there was little nanotube carbon loss (Table 1). Consistently, the O-1s peak of the hCNTs were of higher intensities and/or broader than that of the pristine MWCNT, and exhibited similar increasing trend with longer heating duration resulting in higher peak intensity at the same set temperature (430 °C) (**Figure 3a**). Overall, however, the oxygen contents for all hCNT samples were still quite low (not exceeding ~5% in this work). Therefore, there was little oxidative carbon contributions in their C-1s spectra, with the peak shape very similar to that of the starting MWCNT sample (**Figure 3b**).

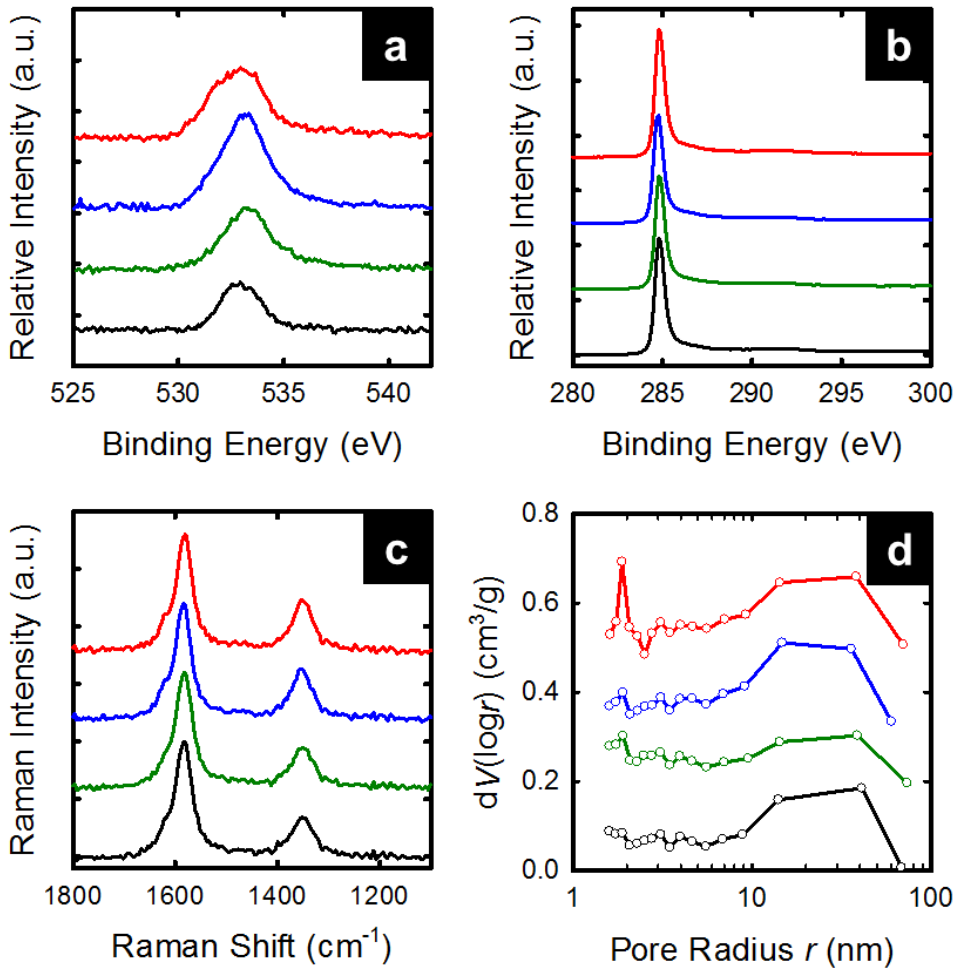

Figure 3. (a) XPS O-1s, (b) XPS C-1s, (c) Raman, and (d) pore distribution plots of various hCNT samples in comparison to those of the pristine MWCNT. From top to bottom in each plot: $hCNT_{430\text{-}10}$ (red), $hCNT_{430\text{-}3}$ (blue), $hCNT_{430\text{-}1}$ (green), pristine MWCNT (black).

Despite the very defective appearance of the hCNTs especially those with high hole yields, their Raman spectra were also very similar to that of the starting MWCNT (**Figure 3c**), with only slightly increased D/G peak ratios for all samples investigated (Table 1). For carbon nanomaterials including CNTs and graphene, it is known that the intensity of G peak (~1580 cm^{-1}) and D peak (~1350 cm^{-1}) qualitatively reflect the relative abundance of sp^2 (graphitic) and sp^3 (defect or edge) carbons, respectively. Therefore, the hCNTs only exhibited a small increase of

sp^3 carbons. Two aspects can be considered. First, the remaining nanotube wall carbons in hCNTs were of high graphitic nature (would have reduced D/G ratio), as a consequence from the preferential removal of defective carbons in the partial air oxidation process. On the other hand, there were plenty of newly created nanotube edge carbons at the holes (would have increased D/G ratio) as a result of etching. These two aspects largely canceled each other out, with the latter in slight dominance and thus overall slightly increased D/G peak ratios.

The opening of the nanotube inner cavity via hole generation was best reflected by the significant increase of BET surface area of hCNTs in comparison to the pristine MWCNT (Table 1). For example, the BET surface area values of $hCNT_{430\text{-}10}$ and $hCNT_{480\text{-}1}$ were 56.1 and 75.7 m^2/g, respectively, in comparison to 33.4 m^2/g for the pristine MWCNT. The pore volume for hCNTs (estimated using the BJH method) also significantly improved from pristine MWCNTs. For example, the BJH pore volumes for the above mentioned three samples were 0.246, 0.289, and 0.199 cm^3/g, respectively. **Figure 3d** further shows the pore distribution plots for the three hCNT samples obtained at 430 °C with different heating durations in comparison to that of the pristine MWCNT sample. While the mesopore (> 10 nm) volume was of little change for all hCNT samples, the micropore volume (< 2 nm) for the $hCNT_{430\text{-}10}$ exhibited a drastic increase as shown by the presence of a sharp peak. These observations were quite different from the nitrogen adsorption-desorption behavior of holey graphene from a similar catalyst-free air oxidation process.[22] In that case, BET surface area and pore volume of holey graphene were only slightly increased from the starting graphene, while the micropore fraction disappeared upon hole generation but with an increase in mesopore fraction. In the case of hCNT vs. MWCNT presented here, the inner surfaces of nanotube cavity became accessible after hole generation. In the case of holey graphene vs. graphene, however, no new surface area was generated. The

observed gas adsorption behavior changes were most likely attributed to the change of stacking behavior of the highly exfoliated graphene sheets upon air oxidation, which are likely minimal for the current nanotube samples that were dense powders.

The electrochemical properties of hCNTs were characterized using a conventional 3-electrode setup with aqueous KOH solution (6 M) as the electrolyte. hCNTs obtained at a moderate set temperature of 430 °C but with different heating durations (1, 3, and 10 h) were selected as examples to illustrate the effect of generated holes. Cyclic voltammetry (CV) plots at the same scanning rate of 100 mV/s for the three hCNT samples are shown in **Figure 4a** and are compared with that of the pristine MWCNT sample. The y-axis was normalized to specific capacitance C_m using $C_m = I_m / (dV/dt)$, where I_m is the measured current density and dV/dt is the scan rate. All plots were of similar near-rectangular shapes, suggesting that the charge storage was dominated by electrical double-layer behavior. $hCNT_{430\text{-}1}$ only exhibited slight increase in capacitance performance in comparison to the control. However, the two hCNT samples with longer heating durations, especially $hCNT_{430\text{-}10}$, exhibited significant improvement in capacitance.

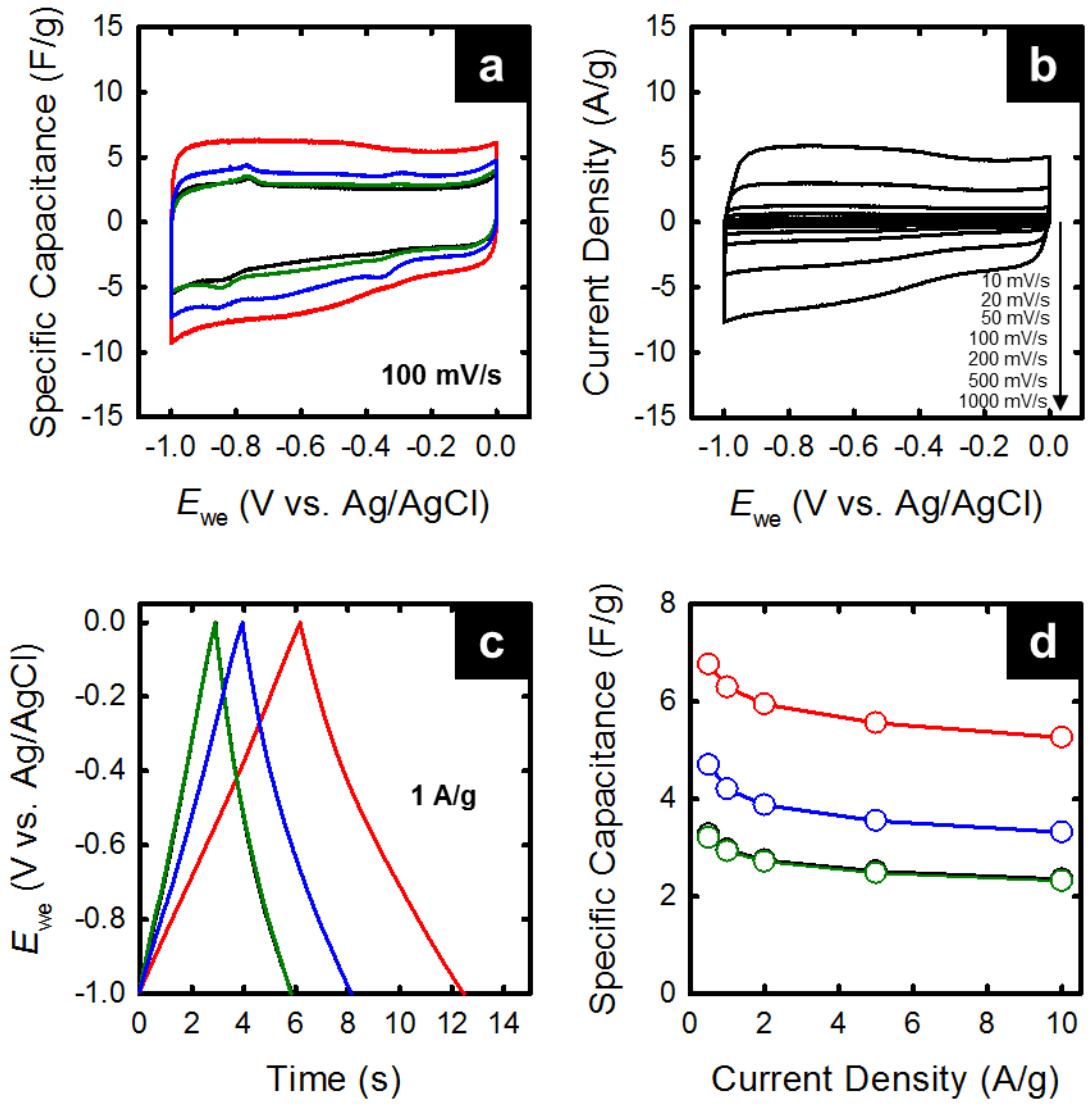

Figure 4. Electrochemical capacitive properties of hCNTs. (a) CV plots at a scan rate of 100 mV/s of $hCNT_{430\text{-}10}$ (red), $hCNT_{430\text{-}3}$ (blue), $hCNT_{430\text{-}1}$ (green), in comparison to that of pristine MWCNTs. (b) CV plots of $hCNT_{430\text{-}10}$ at various scan rates (from inside out: 10, 20, 50, 100, 200, 500, and 1000 mV/s). (c) Galvanometric charge-discharge plots at a current density of 1 A/g and (d) the dependence of specific capacitance on current density for the same three samples.

Such improvement could be readily attributed to the presence of holes that exposed inner walls of the nanotubes to the access of electrolyte molecules. This effect was much less pronounced in $hCNT_{430\text{-}1}$ and absent in the pristine MWCNT sample. The exposure of nanotube

inner walls in $hCNT_{430\text{-}3}$ and $hCNT_{430\text{-}10}$ samples resulted in *de facto* multi-layered graphene sheets in segments of the nanotubes, where both sides of conjugated carbon surface could be used to form electrical double-layer and thus contribute to the charge storage. Consistently, the C_m plateau of $hCNT_{430\text{-}10}$ with effective hole formation was approximately twice as high as that of the pristine MWCNT (Figure 4a), suggesting majority of the inner cavity became accessible. In addition, the hCNT samples with prolonged heating duration had higher oxygen contents (Table 1 and Figure 3a) in the form of oxygen functional groups that were likely enriched at the hole edges, allowing further capacitance improvement.[22]

In Figure 4a, there were two small peaks in both oxidation and reduction scan directions for $hCNT_{430\text{-}1}$, $hCNT_{430\text{-}3}$, and the pristine MWCNT, which could be readily attributed to the residual iron catalysts. Consistent with TGA results, these peaks became absent in the CV plot of $hCNT_{430\text{-}10}$ since the catalysts were largely removed after hole generation and acid purification (Table 1). The rate performance of $hCNT_{430\text{-}10}$ was further evaluated via CV measurements at different scan rates. As shown in **Figure 4b**, all CV plots of $hCNT_{430\text{-}10}$ at scan rates in the range of 10 mV/s – 1 V/s exhibited typical rectangle shapes with no distortion, suggesting ultrafast charge storage mechanism of a high-rate electrical double layer capacitive material.

Shown in **Figure 4c** are the galvanostatic charge-discharge plots for the hCNT samples and the pristine MWCNT sample at a current density of 1 A/g. All plots were highly symmetrical and of triangular shapes, consistent with the notion that electrical double-layer capacitive behavior was dominant. While $hCNT_{430\text{-}1}$ had nearly identical charge-discharge properties to the control, $hCNT_{430\text{-}3}$ and $hCNT_{430\text{-}10}$ exhibited significantly longer charge and discharge time, indicating higher capacitance values for these two samples. All these results were consistent with the CV data. Specific capacitance values of the hCNT samples were directly calculated from the

discharge time by using $C_m = I_m \Delta t/\Delta V$, where I_m is the current density used, Δt is the discharge time measured, ΔV is the voltage window. At I_m = 1 A/g, the C_m values for $hCNT_{430\text{-}1}$, $hCNT_{430\text{-}3}$, and $hCNT_{430\text{-}10}$ were 2.9, 4.2, and 6.3 F/g, respectively, in comparison to 2.9 F/g of the pristine MWCNT sample. This trend ($hCNT_{430\text{-}10}$ > $hCNT_{430\text{-}3}$ > $hCNT_{430\text{-}1}$ ≈ MWCNT in C_m) was consistent at various I_m up to 10 A/g measured in this study (**Figure 4d**). At higher I_m, the C_m values for all samples were only slightly smaller. The $hCNT_{430\text{-}10}$ sample exhibited the highest capacitance retention percentage, i.e., the best rate performance.

C_m values for hCNTs obtained at other conditions used in this study were also measured (Table 1). Most of these values were similarly much improved in comparison to the pristine MWCNTs. The synthesis data and physical properties of all samples in Table 1 generally supported the proposed mechanism that higher surface area and higher oxygen content were responsible for the capacitance improvement. Another parameter that likely contributed to the capacitance improvement was the pore volume, which were largely attributed to the increase in the micropore component as seen in Figure 3d. The C_m values were also plotted against the hole yield for all samples studied in this work (**Figure 5**). Interestingly, the capacitance exhibited an increasing trend with the hole yield up ~50%, when the hole generation dominated the nanotube morphology change in air oxidation. Further increase in the hole yield value led to significant nanotube loss; as a result, the C_m values started to decrease.

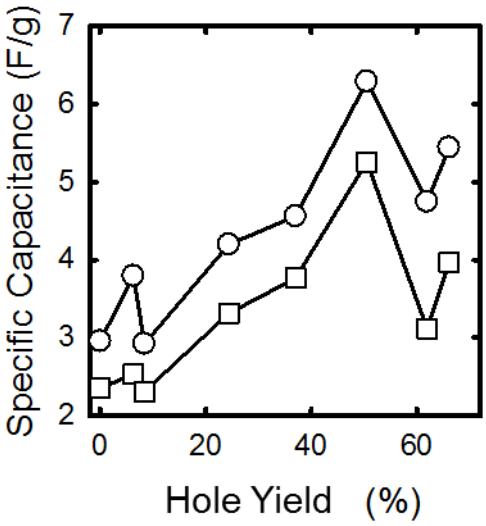

Figure 5. Dependence of specific capacitance values measured at 1 A/g (○) and 10 A/g (□) on the hole yield for all hCNT samples studied in this work.

Conclusions

hCNTs were prepared in a facile air oxidation process without added catalysts. Mechanistically, the hole generation was initiated by the catalyst-free oxidation of nanotube surface defect carbons. The initial opening of inner cavity allowed oxygen access to the encapsulated catalyst, which induced the generation of much larger openings through the nanotube walls. Higher temperature and longer duration were in favor of hole generation, but over-oxidation led to nanotube shortening and significant material loss. hCNTs with opened inner cavities exhibited enhanced surface area, pore volume and oxygen content, which led to much improved electrochemical capacitive performance.

Because the hole formation was initiated in a catalyst-free process, the current method should be universal and generally applicable to most types of CNTs, regardless of their wall thicknesses and catalyst contents. However, it is important to ensure the optimization of the

oxidation conditions to generate the desirable extent of hole formation for inner cavity exposure while minimizing over-oxidation. As a new family member of "holey nanomaterials", hCNTs are expected to have broad applications not only in energy storage, but also in catalysis, sensors, membranes, and biomolecular and drug delivery.

Acknowledgements. Financial supports from the Leading Edge Aeronautics Research for NASA (LEARN) program (Grant No. NNX13AB88A) and NASA Langley Internal Research and Development (IRAD) Program are gratefully acknowledged. C.J.C. was a Langley Aerospace Research Summer Scholars (LARSS) Program scholar supported by LEARN.

References:

[1] Zhai, Y.; Dou, Y.; Zhao, D.; Fulvio, P. F.; Mayes, R. T.; Dai, S. Carbon Materials for Chemical Capacitive Energy Storage. *Adv. Mater.* **2011**, *23*, 4828-4850.

[2] Jariwala, D.; Sangwan, V. K.; Lauhon, L. J.; Marks, T. J.; Hersam, M. C. Carbon Nanomaterials for Electronics, Optoelectronics, Photovoltaics, and Sensing. *Chem. Soc. Rev.* **2013**, *42*, 2824-2860.

[3] Georgakilas, V.; Perman, J. A.; Tucek, J.; Zboril, R. Broad Family of Carbon Nanoallotropes: Classification, Chemistry, and Applications of Fullerenes, Carbon Dots, Nanotubes, Graphene, Nanodiamonds, and Combined Superstructures. *Chem. Rev.* **2015**, *115*, 4744-4822.

[4] Worsley, M. A.; Pauzauskie, P. J.; Olson, T. Y.; Biener, J.; Satcher, J. H.; Baumann, T. F. Synthesis of Graphene Aerogel with High Electrical Conductivity. *J. Am. Chem. Soc.* **2010**, *132*, 14067-14069.

[5] Jiang, L.; Fan, Z. Design of Advanced Porous Graphene Materials: From Graphene Nanomesh to 3D Architectures. *Nanoscale* **2014**, *6*, 1922-1945.

[6] Zhang, X.; Zhang, H.; Li, C.; Wang, K.; Sun, X.; Ma, Y. Recent Advances in Porous Graphene Materials for Supercapacitor Applications. *RSC Adv.* **2014**, *4*, 45862-45884.

[7] Han, S.; Wu, D.; Li, S.; Zhang, F.; Feng, X. Porous Graphene Materials for Advanced Electrochemical Energy Storage and Conversion Devices. *Adv. Mater.* **2014**, *26*, 849-864.

[8] Xin, S.; Guo, Y.-G.; Wan, L.-J. Nanocarbon Networks for Advanced Rechargeable Lithium Batteries. *Acc. Chem. Res.* **2012**, *45*, 1759-1769.

[9] Lin, Z.; Zeng, Z.; Gui, X.; Tang, Z.; Zou, M.; Cao, A. Carbon Nanotube Sponges, Aerogels, and Hierarchical Composites: Synthesis, Properties, and Energy Applications. *Adv. Energy Mater.* **2016**, *6*, 1600554.

[10] Bordjiba, T.; Mohamedi, M.; Dao, L. H. New Class of Carbon-Nanotube Aerogel for Electrochemical Power Sources. *Adv. Mater.* **2008**, *20*, 815-819.

[11] Zou, J.; Liu, J.; Karakoti, A. S.; Kumar, A.; Joung, D.; Li, Q.; Khondaker, S. I.; Seal, S.; Zhai, L. Ultralight Multiwalled Carbon Nanotube Aerogel. *ACS Nano* **2010**, *4*, 7293-7302.

[12] Yang, J.; Ma, M.; Li, L.; Zhang, Y.; Huang, W.; Dong, X. Graphene Nanomesh: New Versatile Materials. *Nanoscale* **2014**, *6*, 13301-13313.

[13] Lin, Y.; Liao, Y.; Chen, Z.; Connell, J. W. Holey Graphene: A Unique Structural Derivative of Graphene. *Mater. Res. Lett.* **2017**, in press.

[14] Han, T. H.; Huang, Y.-K.; Tan, A. T. L.; Dravid, V. P.; Huang J. Steam Etched Porous Graphene Oxide Network for Chemical Sensing. *J. Am. Chem. Soc.* **2011**, *133*, 15264-15267.

[15] Zhao, X.; Hayner, C. M.; Kung, M. C.; Kung, H. H. In-Plane Vacancy-Enabled High-Power Si-Graphene Composite Electrode for Lithium-Ion Batteries. *Adv. Energy Mater.* **2011**, *1*, 1079-1084.

[16] Zhao, X.; Hayner, C. M.; Kung, M. C.; Kung, H. H. Flexible Holey Graphene Paper Electrodes with Enhanced Rate Capability for Energy Storage Applications. *ACS Nano* **2011**, *5*, 8739-8749.

[17] Kotchey, G. P.; Allen, B. L.; Vedala, H.; Yanamala, N.; Kapralov, A. A.; Tyurina, Y. Y.; Klein-Seetharaman, J.; Kagan, V. E.; Star, A. The Enzymatic Oxidation of Graphene Oxide. *ACS Nano* **2011**, *5*, 2098-2108.

[18] Lin, Y.; Watson, K. A.; Kim, J.-W.; Baggett, D. W.; Working, D. C.; Connell, J. W. Bulk Preparation of Holey Graphene via Controlled Catalytic Oxidation. *Nanoscale* **2013**, *5*, 7814-7824.

[19] Radich, J. G.; Kamat, P. V. Making Graphene Holey. Gold-Nanoparticle-Mediated Hydroxyl Radical Attack on Reduced Graphene Oxide. *ACS Nano* **2013**, *6*, 5546-5557.

[20] Xu, Y.; Lin, Z.; Zhong, X.; Huang, X.; Weiss, N. O.; Huang, Y.; Duan, X. Holey Graphene Frameworks for Highly Efficient Capacitive Energy Storage. *Nat. Commun.* **2014**, *5*, 4554.

[21] Han, X.; Funk, M. R.; Shen, F.; Chen, Y.-C.; Li, Y.; Campbell, C. J.; Dai, J.; Yang, X.; Kim, J.-W.; Liao, Y.; Connell, J. W.; Barone, V.; Chen, Z.; Lin, Y.; Hu, L. Scalable Holey Graphene Synthesis and Dense Electrode Fabrication toward High-Performance Ultracapacitors. *ACS Nano* **2014**, *8*, 8255-8265.

[22] Lin, Y.; Han, X.; Campbell, C. J.; Kim, J.-W.; Zhao, B.; Luo, W.; Dai, J.; Hu, L.; Connell, J. W. Holey Graphene Nanomanufacturing: Structure, Composition, and Electrochemical Properties. *Adv. Func. Mater*. **2015**, *25*, 2920-2927.

[23] Paul, R. K.; Badhulika, S.; Saucedo, N. M.; Mulchandani, A. Graphene Nanomesh as Highly Sensitive Chemiresistor Gas Sensor. *Anal. Chem.* **2012**, *84*, 8171-8178.

[24] Wang, X.; Jiao, L.; Sheng, K.; Li, C.; Dai, L.; Shi, G. Solution-Processable Graphene Nanomeshes with Controlled Pore Structures. *Sci. Rep.* **2013**, *3*, 1996.

[25] Koenig, S. P.; Wang, L.; Pellegrino, J.; Bunch, J. S. Selective Molecular Sieving through Porous Graphene. *Nat. Nanotechnol.* **2012**, *7*, 728-732.

[26] Cohen-Tanugi, D.; Grossman, J. C. Water Desalination Across Nanoporous Graphene. *Nano Lett.* **2012**, *12*, 3602-3608.

[27] Sun, C.; Wen, B.; Bai, B. Recent Advances in Nanoporous Graphene Membrane for Gas separation and Water Purification. *Sci. Bull.* **2015**, *60*, 1807-1823.

[28] Andrews, R.; Jacques, D.; Qian, D. L.; Rantell, T. Multiwall Carbon Nanotubes: Synthesis and Application. *Acc. Chem. Res.* **2012**, *35*, 1008-1017.

[29] Haddon, R. C.; Sippel, J.; Rinzler, A. G.; Papadimitrakopoulos, F. Purification and Separation of Carbon Nanotubes. *MRS Bull.* **2004**, *29*, 252-259.

[30] Chiang, I. W.; Brinson, B. E.; Smalley, R. E.; Margrave, J. L.; Hauge, R. H. Purification and Characterization of Single-Wall Carbon Nanotubes. *J. Phys. Chem. B* **2001**, *105*, 1157-1161.

[31] Lin, Y.; Kim, J.-W.; Connell, J. W.; Lebron-Colon, M.; Siochi, E. J. Purification of Carbon Nanotube Sheets. *Adv. Eng. Mater.* **2015**, *17*, 674-688.

[32] Zhao, Y.; Hu, C.; Song, L.; Wang, L.; Shi, G.; Dai, L.; Qu, L. Functional Graphene Nanomesh Foam. *Energy Environ. Sci.* **2014**, *7*, 1913-1918.